This is a non-peer reviewed manuscript submitted to *Advances in Water Resources* for potential publication.

A Hybrid Pore-Network-Continuum Modeling Framework for Flow and Transport in 3D Digital Images of Porous Media

Li Zhang[a,b], Bo Guo[a,*], Chaozhong Qin[c,d], Yongqiang Xiong[b]

[a]*Department of Hydrology & Atmospheric Sciences, University of Arizona, Tucson, AZ, USA*
[b]*State Key Laboratory of Organic Geochemistry, Guangzhou Institute of Geochemistry, Chinese Academy of Science, Guangzhou, China*
[c]*State Key Laboratory of Coal Mine Disaster Dynamics and Control, Chongqing University, Chongqing, China*
[d]*School of Resources and Safety Engineering, Chongqing University, Chongqing, China*

Abstract

Understanding flow and transport in multiscale porous media is challenging due to the presence of a wide range of pore sizes. Recent imaging advances offer high-resolution characterization of the multiscale pore structures. However, simulating flow and transport in 3D digital images requires models to represent both the resolved and sub-resolution pore structures. Here, we develop a hybrid pore-network-continuum modeling framework. The hybrid framework treats the smaller pores below the image resolution as a continuum using the Darcy-scale formalism and explicitly represents the larger pores resolved in the images employing a pore network model. We validate the hybrid model against direct numerical simulations for single-phase flow and solute transport and further demonstrate its applicability for simulating two-component gas transport in a shale rock sample. The results indicate that the new hybrid model represents the flow and transport process in multiscale porous media while being much more computationally efficient than direct numerical simulation methods for the range of simulated conditions.

Keywords: Pore network model, Multiscale pore structure, 3D digital images, Hybrid modeling, Continuum

Highlights

- We develop a hybrid pore-network-continuum (h-PNM-continuum) modeling framework.

- It applies to pore-scale flow and transport in 3D multiscale digital images.

- Resolved and sub-resolution pores, and the mass transfer between them are modeled.

- h-PNM-continuum is computationally more efficient than standard direct numerical simulations.

- The hybrid modeling framework can be extended to more complex processes.

*Corresponding author
Email address:* `boguo@arizona.edu` (Bo Guo)

1. Introduction

Pore-scale flow and transport processes in porous materials play a critical role in many geoscience and engineering applications, such as hydrocarbon recovery, CO_2 sequestration, contaminant transport, nuclear waste storage, fuel cells, and biomedical applications. Thanks to advances in imaging technologies and computational modeling, pore-scale imaging and modeling (sometimes referred to as digital rock or soil physics) have become a standard technology to study fluid flow and transport in porous media at microscopic scales (Blunt et al., 2013; Bultreys et al., 2016; Xiong et al., 2016). Advanced imaging and analysis techniques including non-destructive X-ray computed tomography (e.g., micro-CT or nano-CT), focused ion beam–scanning electron microscopy (FIB-SEM), transmission electron microscopy (TEM), and focused ion beam–helium ion microscope (FIB-HIM), have been increasingly used to visualize and quantify 3D pore-scale structures of porous media (e.g., Wildenschild & Sheppard, 2013; Cnudde & Boone, 2013; Elmorsy et al., 2023; Zahasky et al., 2023; Zheng et al., 2017). While imaging characterization can now achieve resolutions down to a few nanometers, digital images often cannot resolve all the pores of porous media with a wide range of pore sizes due to a trade-off between the spatial resolution and the size of the field of view. As a result, "two-scale" digital images—large pores resolved in the image and much smaller sub-resolution pores coexist—arise when applying imaging characterization to various porous media, e.g., shale rocks, carbonates, tight sandstones, coalbed, and soils. These unresolved microporous subdomains have been demonstrated to have a strong impact on the flow and transport processes for many applications (Mehmani & Prodanović, 2014; Bultreys et al., 2015; Scheibe et al., 2015; Soulaine et al., 2016; Guo et al., 2018; Mehmani et al., 2021; Yang et al., 2021), which suggests that they should be accounted for in modeling approaches.

The need to represent flow and transport processes in both scales of these two-scale images poses significant challenges to pore-scale modeling. Pore-scale modeling based on high-resolution images can be generally grouped into two categories (Meakin & Tartakovsky, 2009; Blunt et al., 2013; Xiong et al., 2016; Mehmani et al., 2021; Yang et al., 2016; Gong et al., 2021): (1) direct numerical simulation (DNS) and (2) pore network model (PNM). Both DNS and PNM approaches have been extended to model flow and transport in "two-scale" digital images. Soulaine & Tchelepi (2016) proposed a micro-continuum modeling framework based on the Darcy-Brinkman-Stokes equation (DBS), where the Stokes equation is solved in the resolved pores and Darcy's law is utilized for the fluid flow in the sub-resolution microporous subdomain. Similar DBS-based micro-continuum frameworks have been used and generalized to include various processes, including solute transport (Scheibe et al., 2015), mineral dissolution and reactive transport (Golfier et al., 2002; Soulaine et al., 2017, 2018; Maes & Menke, 2021; You & Lee, 2021; Molins et al., 2021; Maes et al., 2022), gas and multi-fluid transport in shale rocks (Guo et al., 2018; Soulaine et al., 2019; Guo et al., 2019), two-phase flow (Carrillo et al., 2020; Maes & Menke, 2021; Carrillo et al., 2022), fluid-solid interaction and deformation (Carrillo & Bourg, 2019, 2021), and heat transfer (Maes & Menke, 2022; Xu et al., 2022). While the DBS-based micro-continuum model provides a DNS modeling framework for flow and transport in "two-scale" digital images, like any other DNS models, it requires high computation costs when simulating

3

high-resolution digital images of porous materials.

PNM has also been extended in various forms to model the flow and transport processes in "two-scale" porous media. The extensions are often referred to as the dual pore network model (dual PNM). Bekri et al. (2005) presented a dual PNM that simulated mass transfer in a two-scale porous medium, which employed a large-scale network to represent vugs or fractures and a small-scale network for the homogeneous matrix. Bauer et al. (2012) introduces a dual PNM where the large-scale pore network is extracted from images, and micropores function as parallel throats alongside the resolved pore throats. Based on statistical information from the images at different scales, Jiang et al. (2013) employed stochastic methods to create a small-scale pore network, which was then combined with the larger-scale network, resulting in a two-scale network. Mehmani & Prodanović (2014) developed a dual PNM considering different connectivities between the big and small networks, and used the dual PNM to investigate the impact of microporosity on transport in porous media. Prodanović et al. (2015) extended this approach by determining the location of the small-scale pore network based on digital images of porous media samples. Bultreys et al. (2015) developed another dual PNM where the microporous regions are approximated as effective pore throats that can connect with the large-scale pore network in parallel and in serial. de Vries et al. (2017) developed a dual PNM to study the impact of aggregates on solute transport in dual porosity porous media. These methods have provided critical insights into flow and transport processes in multiscale porous media, but they generally require large computation costs due to a large number of network elements (if the pore structures in the microporous regions are explicitly represented) or need to simplify the spatial interconnectivity between the resolved pores and the microporous regions (when the microporous regions are approximated as effective throats).

To address the above-discussed challenges, we present a new hybrid pore-network-continuum modeling framework (h-PNM-continuum). This hybrid framework treats the unresolved smaller pores (sub-resolution microporous regions) as a continuum described by the Darcy-scale formalism, while explicitly representing the flow and transport processes in the larger pores (the resolved pores) using a PNM. The pore network is extracted from the resolved pore subdomain using the watershed-segmentation-based SNOW algorithm developed by Gostick (2017). Additionally, we develop a new algorithm to connect the pore network to the microporous subdomain while extracting the pore network from the 3D image. Building upon the hybrid framework, we present mathematical formulations for single-phase flow, solute transport, and gas transport in nanoporous shale rocks that accounts for the confinement effects of gas flow in nanopores.

2. Hybrid pore-network-continuum modeling framework (h-PNM-continuum)

In this section, we present the key ingredients of the hybrid modeling framework, which include a modified network extraction algorithm that links the extracted pore network to the microporous subdomain, mathematical formulations for single-phase flow, solute transport, and two-component gas transport in shale rocks, and numerical methods used to discretize and solve the governing equations.
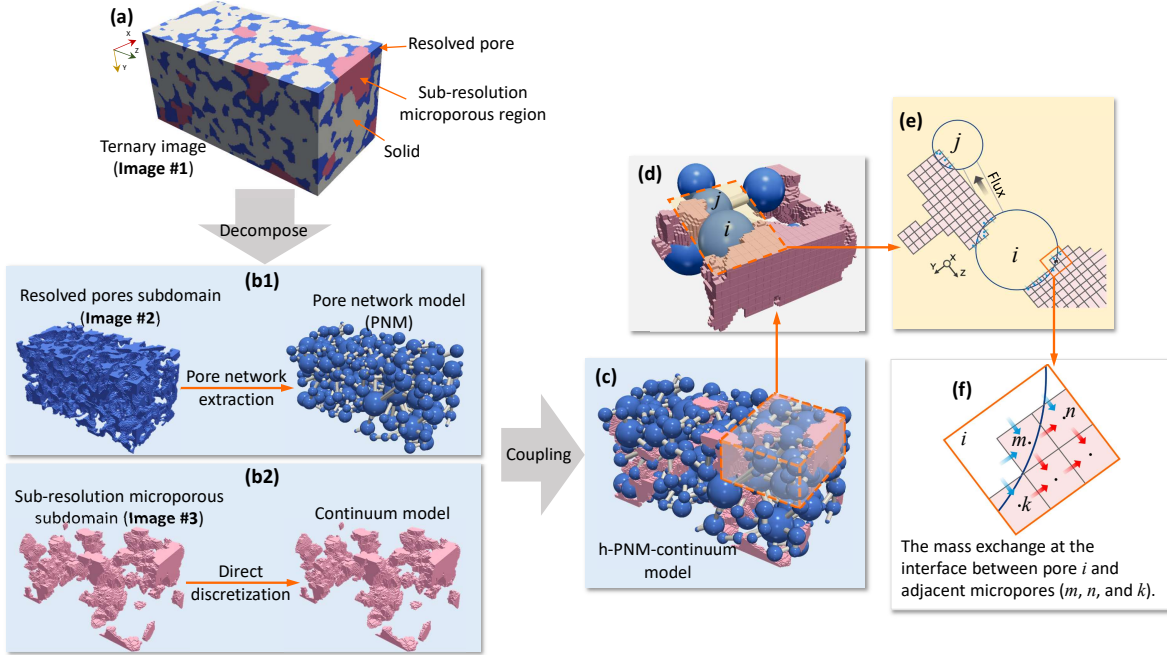
4

Figure 1: Schematic of the hybrid pore-network-continuum modeling framework. (a) A ternary segmented image (Image #1) with blue, pink, and grey colors denoting the resolved pores, sub-resolution microporous regions, and non-porous solids, respectively. (b1) Pore network extraction from the resolved pore subdomain (Image #2). (b2) Numerical discretization of the sub-resolution microporous subdomain (Image #3). (c) The coupled hybrid pore-network-continuum (h-PNM-continuum) representation of the original ternary image. (d) A zoom-in view to illustrate the coupling between the pore network and the discretized continuum subdomain. (e) An example of pores i and j from (d) that are coupled with the discretized continuum subdomain. (f) A zoom-in view of the interface between pore i and the adjacent numerical cells m, n, and k in the continuum subdomain.

2.1. Network extraction and coupling between the pore network and the microporous subdomain

For a ternary segmented image (Image #1) that consists of three subdomains including resolved pores, sub-resolution microporous regions, and solids (Figure 1(a)), we need to extract the pore network from the resolved pore subdomain and then connect the pore bodies to the sub-resolution microporous subdomain based on original connectivity between the two subdomains. We do so by augmenting the watershed-segmentation-based SNOW algorithm developed by Gostick (2017). The augmented algorithm involves two steps: (1) decompose the ternary image to extract the pore network from the resolved pore subdomain (Figure 1(b1)) and discretize the continuum subdomain (Figure 1(b2)); and (2) couple the extracted pore network and the discretized microporous subdomain (Figure 1(c)). We present each step in the following subsections.

2.1.1. Network extraction and discretization

We decompose the ternary image (Image #1) into two binary images (Figure 1): Image #2 containing only the resolved pores and solid, and Image #3 containing only microporous region (i.e., continuum) and

solid. Then, we extract the pore network from Image #2 using the watershed-segmentation-based SNOW algorithm developed by Gostick (2017) (Figure 1(b1)), where we approximate the pore bodies as spheres and pore throats as cylindrical tubes. The SNOW algorithm employs several techniques, including prefiltering the distance map, removing peaks on saddles and plateaus, and merging nearby peaks, to mitigate the peaks and the spurious local maxima resulting from over-segmentation of the standard watershed-segmentation-based algorithms (Rabbani et al., 2014; Gostick, 2017). When applying the SNOW algorithm, a multidimensional Gaussian blur filter with a sigma value of 0.35 is used to smooth the distance map. The radius of the structuring element in the maximum filter is set to 4. The network extraction algorithm provides the volume, coordination number, diameter, and surface area of each pore body, and the diameter, length, and connectivity of each pore throat. Finally, we discretize the microporous subdomain using structure grids (Figure 1(b2)). In the present work, the discretized numerical cells have a one-to-one correspondence to the voxels of the 3D digital image.

2.1.2. Coupling the pore network and the microporous subdomain

To couple the extracted pore network and the discretized microporous subdomain, we identify the voxels of the microporous subdomain residing at the boundary of each pore and subsequently link them to the corresponding extracted pore body. Taking pore i as an example, the coupling process involves the following morphological operations: (1) Dilate the watershed segment of pore i with a spherical structuring element of one-voxel radius. (2) Identify the interface voxels in the overlapping region of the dilated watershed segment of pore i and the microporous region surrounding this pore (we refer to these voxels as the interface voxels for this pore). For example, voxels labeled m, n, k in Figure 1(f) are the interface voxels for pore i. (3) Count the number of side faces of each interface voxel shared with pore i. This is done by dilating the interface voxel and counting the number of dilated voxels overlapped with pore i. (4) Append to pore i the information of its interface voxels, including the total number of interface voxels, the coordinates, and the number of shared faces of each interface voxel. Using the above method, we identify the interface voxels adjacent to each specific pore and finally couple the PNM and the continuum model. The extracted pore network and the coupling between the two submodels (Figure 1(c-f)) are then passed onto a computational framework to simulate flow and transport in two-scale digital images of pore structures.

2.2. Mathematical formulations

The hybrid pore-network-continuum modeling framework can be used to model a wide variety of problems involving fluid flow and transport in two-scale porous media. In the present study, we focus on illustrating three example problems: (1) steady-state incompressible single-phase flow, (2) solute transport, and (3) two-component gas transport in shale. In the following subsections, we present the mathematical formulations for the three examples. Because of the small spatial scales involved, we do not consider gravity.

2.2.1. Steady-state incompressible single-phase flow

For steady-state incompressible single-phase flow, the mass balance equation in a pore body i of the resolved pore subdomain can be written as

$$\sum_{j=1}^{N_i} g_{ij}\left(p_i - p_j\right) + \sum_{m=1}^{M_i} q_{i,m} = 0, \tag{1}$$

where "j" indicates the pore body adjacent to pore body i, and "m" indicates the grid cell in the continuum microporous subdomain that is connected to pore body i. "ij" indicates the pore throat between pore bodies i and j; "i,m" indicates the connection between pore body i and the connected continuum cell m. N_i is the number of pore bodies connected to pore body i. p_i and p_j are the pressure in pore bodies i and j (Pa), respectively. $g_{ij} = \pi d_{ij}^4/(128\mu_{ij}l_{ij})$ is the conductance between pore bodies i and j (m$^4 \cdot$ s/kg), which is derived from Hagen-Poiseuille law for a cylindrical tube, where d_{ij} is the diameter of the pore throat ij (m), μ_{ij} is the gas viscosity (Pa $\cdot$ s) which is determined using the method from Lee et al. (1966), and l_{ij} is the length of the pore throat ij (m). M_i is the number of continuum cells connected to pore body i. $q_{i,m} = k_{i,m}A_{i,m}\left(p_i - p_m\right)/(\mu_{i,m}l_{i,m})$ is the volumetric flux from pore body i to continuum cell m (m^3/s), where $A_{i,m}$ is the area of their interface (m^2), p_m is the pressure in continuum cell m (Pa), $l_{i,m}$ is the distance between pore body i and continuum cell m (m), and $k_{i,m}$ and $\mu_{i,m}$ are the permeability (m^2) and fluid viscosity (Pa $\cdot$ s) at the interface between pore body i and continuum cell m, respectively.

In the continuum microporous subdomain, the mass balance equation for a continuum cell m can be written as

$$\int_{\Omega_m} \nabla \cdot \left(-\frac{k_m}{\mu_m}\nabla p_m\right) dV + \sum_{i=1}^{W_i} q_{m,i} = 0, \tag{2}$$

where Ω_m denotes the integral domain, i.e., the control domain of cell m. The subscript "m,i" indicates the connection between continuum cell m and the connected pore body i. k_m is the the permeability in continuum cell m (m^2). μ_m is gas viscosity in continuum cell m (Pa $\cdot$ s) computed from Lee et al. (1966). W_i is the number of pore bodies connected to continuum cell m. $q_{m,i} = k_{i,m}A_{i,m}\left(p_m - p_i\right)/(\mu_{i,m}l_{i,m})$ is the volumetric flux from continuum cell m to the adjacent pore body i (m^3/s).

2.2.2. Solute transport

This section presents the governing equations for single-phase solute transport processes accounting for advection and dispersion.

For a pore body i, the mass conservation equation of a nonactive solute can be given as

$$V_i\frac{\partial\left(C_i\right)}{\partial t} + \sum_{j=1}^{N_i}\left(g_{ij}\left(p_i - p_j\right)C_{ij} + D_{ij}A_{ij}\frac{C_i - C_j}{l_{ij}}\right) + \sum_{m=1}^{M_i}\left(q_{i,m}C_{i,m} + D_{i,m}A_{i,m}\frac{C_i - C_m}{l_{i,m}}\right) = 0, \tag{3}$$

where V_i is the volume of pore body i (m^3). C_i and C_j are the concentrations in pore bodies i and j (kg/m^3). C_m is the concentration in continuum cell m (kg/m^3). C_{ij} is the concentration in pore throat

ij (kg/m^3), which is assumed to be the upstream concentration between pore bodies i and j. Similarly, $C_{i,m}$ is the upstream concentration at the interface of pore body i and continuum cell m (kg/m^3). $D_{ij} = D_0(1 + \xi Pe^2)$, is the dispersion coefficient in pore throat ij (m^2/s), where D_0 is the molecular diffusion coefficient (m^2/s). The constant ξ depends on the shape of the flow channel (Taylor, 1953); for cylindrical tubes, $\xi = 0.02083$. $Pe = u_{ij}d_{ij}/(2D_0)$ is the local Peclet number (–), where $u_{ij} = g_{ij}(p_i - p_j)/A_{ij}$ is the fluid velocity in the pore throat (m/s) and $A_{ij} = \pi d_{ij}{}^2/4$ is the cross-sectional area of the pore throat (m^2). $q_{i,m} = k_{i,m}A_{i,m}(p_i - p_m)/(\mu_{i,m}l_{i,m})$ is the fluid flux from pore body i to the connected continuum cell m (m^3/s). $D_{i,m}$ is the dispersion coefficient at the interface between pore body i and continuum cell m (m^2/s).

For each continuum microporous cell m, the mass conservation equation is given by

$$V_m\frac{\partial(\phi_m C_m)}{\partial t} + \int_{\Omega_m} \nabla \cdot \left(-\frac{k_m\nabla p_m}{\mu_m}C_m + D_m\nabla C_m\right)dV + \sum_{i=1}^{W_i}\left(q_{m,i}C_{i,m} + D_{i,m}A_{i,m}\frac{C_m - C_i}{l_{i,m}}\right) = 0, \quad (4)$$

where V_m is the volume of continuum cell m (m^3). ϕ_m is the porosity (–). D_m is the dispersion coefficient in continuum subdomain (m^2/s). $q_{m,i} = k_{i,m}A_{i,m}(p_m - p_i)/(\mu_{i,m}l_{i,m})$ is the fluid flux from continuum cell m to pore body i (m^3/s).

2.2.3. Two-component gas transport in shale

We present the governing equations for CO_2 and CH_4 in a shale rock sample with two-scale pore structures. The properties of the bulk gas (i.e., a mixture of CH_4 and CO_2) are functions of both pressure and composition (i.e., the mass fractions of CO_2 and CH_4). Because the majority of the pore space in the continuum subdomain of shale rock is on the order of nanometers, we need to account for the interactions between gas molecules and the solid surface (e.g., pore wall) as well as diffusion of the molecules adsorbed at the solid surface in the continuum models (e.g., Guo et al., 2018). We neglect the adsorption at the solid surfaces and surface diffusion in the resolved pore subdomain due to a relatively small specific surface area of the pore bodies (compared to the continuum microporous subdomain). We need two governing equations for both the pore network and continuum models. One is for the bulk gas, and the other is for one of the components (in this study, CO_2). We select two primary variables, the pressure of bulk gas (p) and the CO_2 mass fraction (ω^{CO_2}).

The mass balance equations for the bulk gas and CO_2 in a pore body i can be written as

$$V_i\frac{\partial\left(\rho_i^b\right)}{\partial t} + \sum_{j=1}^{N_i}\mathcal{J}_{ij}^b + \sum_{m=1}^{M_i}\mathcal{J}_{i,m}^b = 0, \quad (5)$$

$$V_i\frac{\partial(\rho_i^b\omega_i^{CO_2})}{\partial t} + \sum_{j=1}^{N_i}(\mathcal{J}_{ij}^{CO_2,adv} + \mathcal{J}_{ij}^{CO_2,disp}) + \sum_{m=1}^{M_i}\mathcal{J}_{i,m}^{CO_2} = 0, \quad (6)$$

where the superscript "b" denotes bulk gas (i.e., the mixture of CO_2 or CH_4). The superscripts "adv" and "$disp$" denote advection and dispersion, respectively. ρ_i^b is the bulk gas density in pore body i (kg/m^3). $\mathcal{J}_{ij}^b$

8

is the mass flux of bulk gas from pore body i to pore body j (kg/s). $\mathcal{J}_{i,m}^b$ is the mass flux of bulk gas from pore body i to continuum cell m (kg/s). $\omega_i^{CO_2}$ is the mass fraction of CO_2 in pore body i (–). $\mathcal{J}_{ij}^{CO_2,adv}$ and $\mathcal{J}_{ij}^{CO_2,disp}$ are the advective and dispersive mass fluxes of CO_2 from pore body i to j (kg/s), respectively. $\mathcal{J}_{i,m}^{CO_2}$ is the mass flux of CO_2 from pore body i to continuum cell m (kg/s), which includes both advective and dispersive fluxes.

The bulk gas density in both pores and continuum cells can be expressed as

$$\rho^b = \frac{pM^b}{ZRT}, \tag{7}$$

where p is the pressure of bulk gas (Pa). $M^b = M^{CO_2}\varpi^{CO_2} + M^{CH_4}\varpi^{CH_4}$ is molar mass of the bulk gas (kg/mol), where M^{CO_2} and M^{CH_4} are molar mass of CH_4 and CO_2 (kg/mol), respectively; ϖ^{CO_2} and ϖ^{CH_4} ($\varpi^{CO_2} + \varpi^{CH_4} = 1$ in the system) are the mole fraction of CH_4 and CO_2 (–), respectively. T is temperature (K). R is the universal gas constant ($R = 8.314$ kg $\cdot$ m^2/s^2/K/mol). $Z = 0.702e^{-2.5T_r}p_r^2 - 5.524e^{-2.5T_r}p_r + 0.044T_r^2 - 0.164T_r + 1.15$ is the compressibility factor (–), where $T_r = T/T_{crt}$ is the reduced temperature (–) and T_{crt} is the critical temperature (K); $p_r = p/p_{crt}$ is the reduced pressure (–) and p_{crt} is the critical pressure (Pa) (Mahmoud, 2014). In our study, $T_{crt} = T_{crt}^{CO_2}\varpi^{CO_2} + T_{crt}^{CH_4}\varpi^{CH_4}$ and $p_{crt} = p_{crt}^{CO_2}\varpi^{CO_2} + p_{crt}^{CH_4}\varpi^{CH_4}$, where $T_{crt}^{CO_2}$ and $T_{crt}^{CH_4}$ are the critical temperature of CO_2 and CH_4 (K), respectively; $p_{crt}^{CO_2}$ and $p_{crt}^{CH_4}$ are the critical pressure of CO_2 and CH_4 (Pa), respectively.

Here we use a flux model that describes gas flux through cylindrical nanotubes (Beskok & Karniadakis, 1999) to model the flux of the bulk gas through pore throats. The mass flux of the bulk gas and CO_2 can be written as the Hagen-Poiseuille flux q_{H-P} multiplied by a correction factor,

$$\mathcal{J}_{ij}^b = f(Kn)q_{H-P} = f(Kn)g_{ij}\,(p_i - p_j)\rho_{ij}^b, \tag{8}$$

$$\mathcal{J}_{ij}^{CO_2,adv} = J_{ij}^b\omega_{ij}^{CO_2}, \tag{9}$$

where $f(Kn) = (1 + \alpha Kn)\left(1 + 4Kn/\left(1 + 4Kn\right)\right)$ is the correction factor (–). $\alpha = 2\alpha_0/\left(\pi\tan\left(\alpha_1 Kn^\beta\right)\right)$, with $\alpha_0 = 64/15\pi$, $\alpha_1 = 4$, and $\beta = 0.4$. $Kn = \lambda/L$ is the Knudsen number (–), where $\lambda = \mu\sqrt{\pi ZRT}/\left(p\sqrt{2M}\right)$ is the mean free path (m), and L is a characteristic length scale for gas flow (m). In the present study, L is assumed to be equal to the length of the pore throat ij.

The dispersive mass flux of CO_2 can be expressed as

$$\mathcal{J}_{ij}^{CO_2,disp} = \rho_{ij}^b D_{ij}^{CO_2,disp} A_{ij}\frac{\omega_i^{CO_2} - \omega_j^{CO_2}}{l_{ij}}, \tag{10}$$

where ρ_{ij}^b is the bulk gas density in the pore throat ij (kg/m^3). $D_{ij}^{CO_2,disp}$ is the dispersion coefficient of CO_2 in the pore throat ij in the resolved pore subdomain (m^2/s).

The mass fluxes of bulk gas and CO_2 between pore body i and continuum cell m are

9

$$\mathcal{J}_{i,m}^b = \rho_{i,m}^b A_{i,m} \frac{k_{i,m}}{\mu_{i,m}} \frac{p_i - p_m}{l_{i,m}}, \tag{11}$$

$$\mathcal{J}_{i,m}^{CO_2} = J_{i,m}^b \omega_{i,m}^{CO_2} + \rho_{i,m}^b D_{i,m}^{CO_2,disp} A_{i,m} \frac{\omega_i^{CO_2} - \omega_m^{CO_2}}{l_{i,m}}, \tag{12}$$

where $\rho_{i,m}^b$ is the bulk gas density at the interface between pore body i and continuum cell m (kg/m^3). $D_{i,m}^{CO_2,disp}$ is the dispersion coefficient of CO_2 at the interface between between pore body i and continuum cell m (m^2/s), which is approximated using the smaller dispersion coefficients at either side of the interface.

In the continuum microporous subdomain, the mass balance equations for the bulk gas and CO_2 in a continuum cell m can be written as

$$V_m \frac{\partial \left(\phi_m \rho_m^b + \Gamma_m^{CO_2,ex} + \Gamma_m^{CH_4,ex} \right)}{\partial t} + \int_{\Omega_m} \nabla \cdot \left(J_m^b + J_m^{CO_2,sf} + J_m^{CH_4,sf} \right) dV + \sum_{i=1}^{W_i} \mathcal{J}_{m,i}^b = 0, \tag{13}$$

$$V_m \frac{\partial \left(\phi_m \rho_m^b \cdot \omega_m^{CO_2} + \Gamma_m^{CO_2,ex} \right)}{\partial t} + \int_{\Omega_m} \nabla \cdot \left(J_m^{CO_2,adv} + J_m^{CO_2,sf} + J_m^{CO_2,disp} \right) dV + \sum_{i=1}^{W_i} \mathcal{J}_{m,i}^{CO_2} = 0, \tag{14}$$

where "ex" indicates excess adsorption, and "sf" indicates surface diffusion. ρ_m^b is the bulk gas density in continuum cell m (kg/m^3). $\Gamma_m^{CO_2,ex}$ and $\Gamma_m^{CH_4,ex}$ are the excess adsorption of CO_2 and CH_4 per unit volume of bulk porous media (kg/m^3), respectively. J_m^b is the mass flux of bulk gas at the interfaces between continuum cell m and adjacent cells (kg/s/m^2). $J_m^{CO_2,sf}$ is the mass flux of CO_2 by surface diffusion (kg/s/m^2). $J_m^{CH_4,sf}$ is the mass flux of CH_4 (kg/s/m^2) by surface diffusion. $\mathcal{J}_{m,i}^b$ is the mass flux of bulk gas from continuum cell m to pore body i (kg/s). $\omega_m^{CO_2}$ is the mass fraction of CO_2 in continuum cell m (–). $J_m^{CO_2,adv}$ and $J_m^{CO_2,disp}$ are the advective and dispersive mass fluxes of CO_2 at the interfaces between continuum cell m and its adjacent cells (kg/s/m^2), respectively. $\mathcal{J}_{m,i}^{CO_2}$ is the mass flux of CO_2 from continuum cell m to pore body i (kg/s). Other variables and parameters have been defined earlier. Note that $\mathcal{J}_{m,i}^b$ and $\mathcal{J}_{m,i}^{CO_2}$ are only non-zero for continuum cells at the interface between the resolved pore and microporous subdomains.

Adsorption of CO_2 and CH_4 in shales may be described by the Langmuir isotherm (e.g., Zhang et al., 2012; Heller & Zoback, 2014). For a two-component mixture of CO_2 and CH_4, we use the extended multi-component Langmuir isotherm to represent the impact of competitive adsorption. The excess adsorption of CO_2 and CH_4 can be expressed as

$$\Gamma_m^{CO_2,ex} = \Gamma_m^{CO_2,ads} \left(1 - \frac{\omega_m^{CO_2} \rho_m^b}{\omega_m^{CO_2,ads} \rho_m^{ads}} \right), \tag{15}$$

$$\Gamma_m^{CH_4,ex} = \Gamma_m^{CH_4,ads} \left(1 - \frac{\omega_m^{CH_4} \rho_m^b}{\omega_m^{CH_4,ads} \rho_m^{ads}} \right), \tag{16}$$

$$\Gamma_m^{CO_2,ads} = \Gamma_{m,max}^{CO_2} \frac{K_m^{CO_2} p_m \varpi_m^{CO_2}}{1 + K_m^{CO_2} p_m \varpi_m^{CO_2} + K_m^{CH_4} p_m \varpi_m^{CH_4}}, \tag{17}$$

$$\Gamma_m^{CH_4,ads} = \Gamma_{m,max}^{CH_4} \frac{K_m^{CH_4} p_m \varpi_m^{CH_4}}{1 + K_m^{CO_2} p_m \varpi_m^{CO_2} + K_m^{CH_4} p_m \varpi_m^{CH_4}}, \tag{18}$$

where "ads" indicates adsorption. $\Gamma_{m,max}^{CO_2}$ and $\Gamma_{m,max}^{CH_4}$ are the maximum adsorption of CO_2 and CH_4 (kg/m^3), respectively. $K_m^{CO_2}$ and $K_m^{CH_4}$ are the Langmuir coefficients of CO_2 and CH_4 (m $\cdot$ s^2/kg), respectively. $\omega_m^{CH_4} = 1 - \omega_m^{CO_2}$ is the mass fraction of CH_4 in continuum cell m (–). $\omega_m^{CO_2,ads} = \Gamma_m^{CO_2,ads}/(\Gamma_m^{CO_2,ads} + \Gamma_m^{CH_4,ads})$ and $\omega_m^{CH_4,ads} = \Gamma_m^{CH_4,ads}/(\Gamma_m^{CO_2,ads} + \Gamma_m^{CH_4,ads})$ are the mass fractions of CO_2 and CH_4 in the adsorbed phase (–), respectively. ρ_m^{ads} is the adsorbed gas density, which is assumed to be constant (1,000 kg/m^3) (Zhang et al., 2020).

The mass fluxes of the bulk gas and CO_2 in the continuum cell m can be expressed as

$$J_m^b = -\rho_m f(Kn) \frac{k_m}{\mu_m^b} \nabla p_m, \tag{19}$$

$$J_m^{CO_2,adv} = J_m^b \omega_m^{CO_2}. \tag{20}$$

The adsorbed gas can migrate along the pore wall, which causes the surface diffusion process (Ruthven, 1984; Medved and Cerny, 2011). The surface diffusive fluxes of the bulk gas and CO_2 can be expressed as

$$J_m^{CO_2,sf} = -D_m^{CO_2,sf} \nabla \Gamma_m^{CO_2,ads}, \tag{21}$$

$$J_m^{CH_4,sf} = -D_m^{CH_4,sf} \nabla \Gamma_m^{CH_4,ads}, \tag{22}$$

where $D_m^{CO_2,sf} = D_0^{CO_2,sf}/\tau$ and $D_m^{CH_4,sf} = D_0^{CH_4,sf}/\tau$ are the surface diffusion coefficients of CO_2 and CH_4 (m^2/s) in the continuum microporous subdomain, where $D_0^{CO_2,sf}$ and $D_0^{CH_4,sf}$ are surface diffusion coefficients of CO_2 and CH_4 on flat solid surfaces (m^2/s), respectively.

Similarly, we consider component dispersion in the continuum subdomain. The dispersive flux of CO_2 can be expressed as

$$J_m^{CO_2,disp} = -\phi_m \rho_m^b D_m^{CO_2,disp} \nabla \omega_m^{CO_2}, \tag{23}$$

where $D_m^{CO_2,disp}$ is the dispersion coefficient of CO_2 in continuum cell m (m^2/s).

The flux of the bulk gas and CO_2 at the interface between pore i and continuum cell m can be expressed as

$$\mathcal{J}_{m,i}^b = \rho_{i,m}^b A_{i,m} \frac{k_{i,m}}{\mu_{i,m}} \frac{p_m - p_i}{l_{i,m}}, \tag{24}$$

$$\mathcal{J}_{m,i}^{CO_2} = \mathcal{J}_{m,i}^b \omega^{CO_2} + \phi_m \rho_{i,m}^b D_{i,m}^{CO_2,disp} A_{i,m} \frac{\omega_m - \omega_i}{l_{i,m}}. \tag{25}$$

Note that we do not consider the surface diffusion at the interface between pore i and continuum cell m.

11

2.3. Numerical methods

We apply a fully implicit numerical framework to solve the mathematical formulations of the h-PNM-continuum models presented in Section 2.2. The continuum porous domains are discretized in space using the cell-centered finite volume method. The advection term in the solute transport equations (Eqs. 3 & 4) is discretized using a first-order upwinding scheme. The nonlinear equations resulting from the fully implicit discretization are solved using the Newton-Raphson iteration method. Our implementation of the numerical methods employs the automatic differentiation and gridding utilities in the MATLAB Reservoir Simulation Toolbox (Lie, 2019).

We conduct simulations using existing DNS models implemented in the open-source code OpenFOAM to evaluate the accuracy of the first two mathematical formulations of the h-PNM-continuum models. The DNS results for the steady-state single-phase flow are obtained using the simpleFoam solver based on the SIMPLE (Semi-Implicit Method for Pressure Linked Equations) algorithm. The single-phase solute transport DNS results are conducted using the scalarTransportFoam solver.

The initial and boundary conditions for both the h-PNM-continuum and DNS models of each specific test case are presented in Sections 3.1–3.3.

3. Results

We conduct numerical experiments to evaluate the h-PNM-continuum modeling framework for each of the mathematical formulations: (1) steady-state single-phase flow, (2) solute transport process, and (3) compositional single-phase flow in shale. The following three subsections present the details of the problem setup and simulation results.

3.1. Steady-state single-phase flow

We simulate steady-state single-phase flow in a 3D digital image of sintered glass beads and compare the simulations to DNS. To analyze the contribution of the continuum subdomain to the flow behavior in the entire domain, we consider two cases: (1) flow in the whole domain including both the resolved pore and the sub-resolution microporous subdomains, and (2) flow only in the resolved pore subdomain.

The physical size of the domain is 0.0025 m $\times$ 0.0025 m $\times$ 0.01 m in x, y, and z with $100 \times 100 \times 400$ voxels, respectively. We apply the SNOW algorithm to decompose the solid regions within the digital images, and then we label one out of five as the continuum microporous region, creating a ternary digital image. The unresolved pore space in the continuum microporous subdomain accounts for 8.8% of the total pore space in the ternary image. The continuum subdomain is assumed to be homogeneous and isotropic with a porosity of $\phi_m = 0.2$ and a permeability of $k_m = 3$ Darcy (1 Darcy $\approx 9.869 \times 10^{-13}$ m^2). For both the h-PNM-continuum and DNS models, the porosity of the resolved pore subdomain is 0.278 and the total porosity of the entire domain is 0.304. The fluid is assumed incompressible and is described by Eqs. (1–2). The initial pressure of the domain is set to 10 Pa. The inlet and outlet boundaries have a fixed pressure of

Table 1: Computed permeability of the entire domain and the resolved pore subdomain by the h-PNM-continuum model and DNS method.

Model		Permeability (m²)
h-PNM-continuum model	k^{pore}	6.15×10^{-11}
	k	6.61×10^{-11}
DNS method	k^{pore}	5.39×10^{-11}
	k	5.98×10^{-11}

$p_{inlet} = 10$ Pa and $p_{outlet} = 0$, respectively, imposing a gradient pressure from the inlet to the outlet. The other four faces of the domain are closed and set as no flux boundaries. For the hybrid-PNM-continuum model, an absolute tolerance of 10^{-5} for the numerical residual is used as a convergence criterion for the nonlinear Newton-Raphson iterations. For the DNS, the absolute tolerance is 10^{-10} for the SIMPLE solver.

The overall permeability of the entire domain can be computed using Darcy's law as

$$k = \frac{Q\mu L}{A\triangle p} \tag{26}$$

where Q is the volumetric flow rate at the inlet and outlet of the domain (m³/s) at steady state. $L = L_z$ is the length of the domain along the flow direction (m). $A = L_x \times L_y$ is the cross-sectional area of the domain m². $\triangle p = p_{inlet} - p_{outlet}$ is the pressure drop between inlet and outlet.

The computed overall permeability of the entire domain is 6.61×10^{-11} m² from the h-PNM-continuum model and 5.98×10^{-11} m² from the DNS model (Table 1). The computed permeability of the resolved pore subdomain is 6.15×10^{-11} m² and 5.39×10^{-11} m² from the PNM and DNS models, respectively. The permeability calculated from the two models is generally in good agreement. Meanwhile, some discrepancies between the two models are observed, which can be primarily attributed to the differences in the resolved pore subdomain. The higher permeability from the h-PNM-continuum model may result from the simplification of the extracted pore network from the digital images by approximating the pore space as cylindrical pore throats and spherical pore bodies. This is a known issue of image-based pore-network modeling. Multiple more advanced approaches have been developed in the literature to improve the accuracy of PNM for image-based pore-scale simulations, including Zhao et al. (2020), and Raeini et al. (2017, 2018). These enhanced PNM approaches can be incorporated into our h-PNM-continuum framework to improve accuracy.

The spatial distributions of pressure from the h-PNM-continuum model and DNS at steady state are presented in Figure 2. The results show that the pressure fields of both the resolved pore subdomain and unresolved microporous subdomain from the h-PNM-continuum model agree well with the DNS results (columns 1 and 2), which further demonstrates the accuracy of the h-PNM-continuum model for simulating steady-state flow.
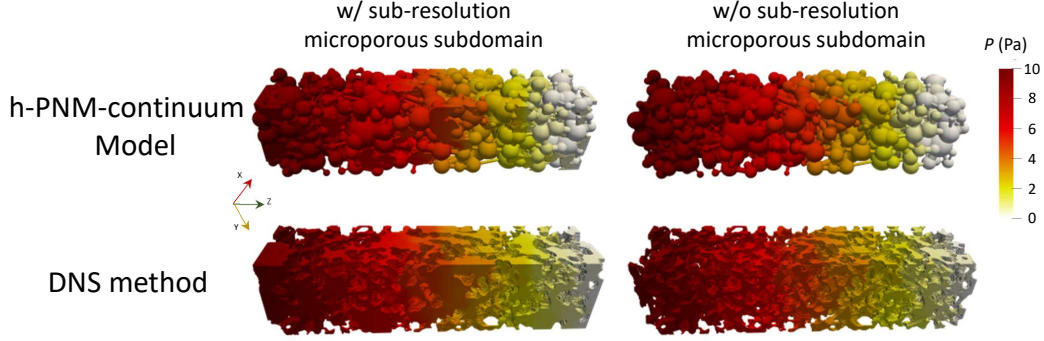
Figure 2: Simulated pressure distributions in the sintered glass beads by the h-PNM-continuum model (row 1) and DNS method (row 2) assuming steady-state. The plots on the left included sub-resolution microporous subdomain, while the plots on the right did not.

3.2. Solute transport

We conduct numerical experiments to simulate the transport of a nonreactive solute under steady-state water flow using the same digital pore-scale image from Section 3.1. To verify the developed model under different flow conditions, we conduct simulations under both low and high Peclet numbers (i.e., $Pe = 0.1$ and 100) and compare the results with that of the DNS method. The Peclet number is defined as

$$Pe = \frac{L_c u}{\phi_e D_0},\tag{27}$$

where L_c is a characteristic length (m), which is set to L_z. $u = k\triangle p/(\mu L_z)$ is the average water flow velocity (m/s). ϕ_e is the effective porosity of the entire domain. D_0 is the molecular diffusion coefficient in the resolved pore subdomain and is set to 2.295×10^{-9} m$^2/s$ (which is equal to the self-diffusion coefficient of neat water at 298.15 K).

The pressure drop between the inlet and the outlet $\triangle p$ is set to 0.1057 Pa and 105.7 Pa to generate the low and high Peclect number scenarios. For solute transport, the initial concentration of the solute is zero. At time $t = 0$, continuous injection of the solute at a concentration of 10 (mol/L) is applied to the inlet. At the outlet boundary, the normal gradient of the solute concentration is set to zero.

For convenience, we define a dimensionless time as

$$T = \frac{Qt}{\phi_e L_x L_y L_z},\tag{28}$$

where the definition of Q, ϕ_e, L_x, L_y, and L_z are consistent with the above definitions.

In Figure 3, we present the 3D concentration distribution of the entire domain for snapshots in time from two models at low and high Peclet numbers ($Pe = 0.1$ vs. $Pe = 100$). The breakthrough curves (BTCs) of the entire domain for the two Peclet numbers are presented in Figure 4. The spatial concentration distribution and BTCs results show that the h-PNM-continuum model matches well with the DNS model for both the low and high Peclet numbers cases.
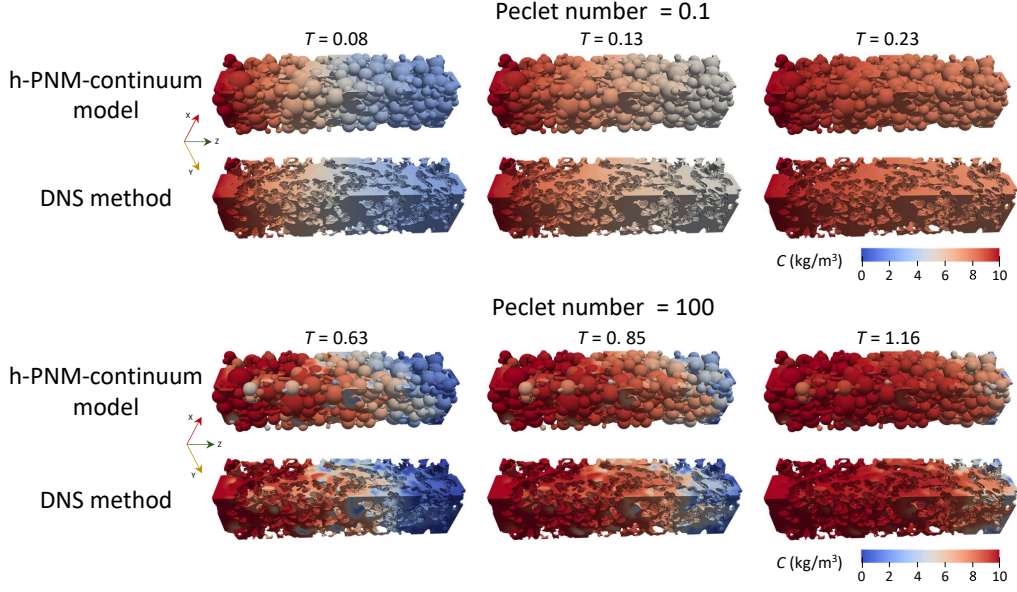
14

Figure 3: Comparison of the spatial distribution of the solute concentration in the sintered glass beads simulated by the h-PNM-continuum model (rows 1 & 3) and DNS method (rows 2 & 4) at low and high Peclet numbers (i.e., $Pe = 0.1$ and 100, respectively).

For the low Peclet number case, the solute transport is dominated by diffusion and dispersion. Under this condition, the assumption of well-mixed solute in each pore body employed by the PNM is reasonable. As a result, excellent agreement between the h-PNM-continuum model and the DNS method is observed for both concentration distributions at different times ($T = 0.08$, 0.13, and 0.23) and the BTCs at the outlet. For the high Peclet number case, advection becomes dominant. From the spatial distribution of the solute concentration, we can see that the plume from the developed h-PNM-continuum model transports slightly faster than the corresponding DNS method. This is because the pore network model assumes a well-mixed condition in each pore body and it has a greater permeability in the resolved pore structure than that computed by the DNS model, both of which lead to faster transport of the solute in the domain. However, even for a high Peclet number regime of Pe=100, the h-PNM-continuum model still appears to provide reliable results compared to direct numerical simulations.

3.3. Compositional single-phase flow

In the third set of numerical experiments, we simulate the injection of CO_2 into a shale sample reconstructed from images obtained using FIB-SEM. The sample is 250 nm $\times$ 250 nm $\times$ 1,000 nm in three dimensions, and the voxel size is 5 nm $\times$ 5 nm $\times$ 5 nm. Voxels in the digital 3D image are segmented into four constituents: resolved pore space, organic matter, clay, and granular minerals. The organic matter and clay regions are represented by the continuum (i.e., the unresolved microporous region), while the granular minerals are assumed non-porous solid impermeable to flow. We use the methods described in Section 2.1 to extract and couple the pore network and the continuum grid cells. We simulate two scenarios to examine the
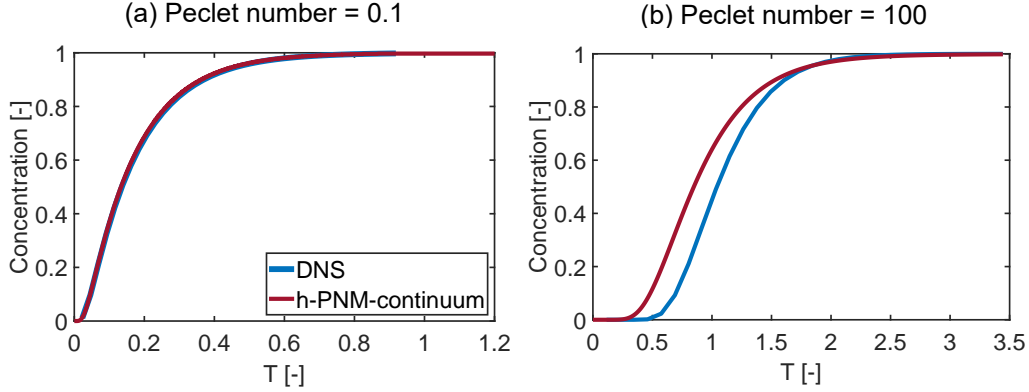
15

Figure 4: Comparisons of outflow concentration simulated using the h-PNM-continuum model (red curves) and the DNS method (blue curves) at low and high Peclet numbers ($Pe = 0.1$ and 100, respectively).

contribution of the continuum subdomain to CH_4 production. One considers the entire domain, including the unresolved microporous regions and the other focuses on the resolved pore subdomain only.

For the numerical simulations, the h-PNM-continuum model solves the governing equations described in Section 2.2.3 (Eqs. 5, 6, 13 & 14). We assume that all of the pore space in the shale sample is initially occupied by CH_4 (i.e., $\omega^{CO_2} = 0$) at a gas pressure of 10 MPa and a temperature of 400 K. At the inlet boundary (where $z = 0$), we continuously inject CO_2 (i.e., $\omega^{CO_2} = 1$) at a fixed pressure of 10.1 MPa. At the outlet boundary (where $z = 1,000$ nm), the pressure is fixed to 10 MPa while the CO_2 mass fraction is set as zero-gradient (i.e., $\partial\omega^{CO_2}/\partial z|_{\text{outlet}} = 0$). Other parameters used in the simulations are presented in Table 2.

We define a characteristic time scale t_c and use it to define a dimensionless time $T = t/t_c$. t_c is the time when half of the total CH_4 in the entire domain is displaced by CO_2. The spatial distribution of the CO_2 mass fraction and cross-section-averaged mass fraction of CO_2 and CH_4 along the z-direction are presented in Figure 5. The gas pressure in the domain reaches equilibrium relatively quickly (at approximately $T = 0.0012$). However, the transport of the CO_2 and CH_4 components lasts much longer. It is interesting that the transport of CO_2 is faster in the presence of the sub-resolution microporous subdomain (Figure 5). This is because the microporous subdomain increases the connectivity of the resolved pores, resulting in improved effective connectivity across the entire domain. Comparison of Figure 5 rows 1 & 2, we can see that the isolated pores are connected by the sub-resolution microporous regions within the whole domain. For real shale rocks, the connectivity of resolved pores is usually limited, while sub-resolution micropores in organic matter and clay minerals have the potential to provide storage spaces and migration pathways for hydrocarbons.

The displacement of CH_4 by the injected CO_2 can also be measured by the mass flow rate of the two components at the outlet boundary. In Figure 6(a), we observe a significantly advanced arrival of CO_2 when microporous subdomain is coupled with the pore network (simulated using the h-PNM-continuum

16

Table 2: Parameters used for the simulations of CO_2 injection into a shale sample.

Parameter	Value
Permeability of the continuum subdomain (k_m)	0.5 nanoDarcy
Porosity of the continuum subdomain (ϕ_m)	0.1
Langmuir adsorption coefficient for CO_2 ($K_m^{CO_2}$) [1]	1×10^{-7} m $\cdot$ s^2/kg
Langmuir adsorption coefficient for CH_4 ($K_m^{CH_4}$) [1]	1.7×10^{-7} m $\cdot$ s^2/kg
Maximum adsorption of CO_2 ($\Gamma_{m,max}^{CO_2}$) [1]	45 kg/m^3
Maximum adsorption of CH_4 ($\Gamma_{m,max}^{CH_4}$) [1]	5 kg/m^3
Surface diffusion coefficient for CO_2 on flat solid surface ($D_0^{CO_2,sf}$) [2]	3.135×10^{-8} m^2/s
Surface diffusion coefficient for CH_4 on flat solid surface ($D_0^{CH_4,sf}$) [2]	1.14×10^{-8} m^2/s
Dispersion coefficient of CO_2 in the continuum subdomain ($D_m^{CO_2,disp}$) [1]	1×10^{-9} m^2/s
Dispersion coefficient of CO_2 in the pore throat ($D_{ij}^{CO_2,disp}$) [3]	2×10^{-8} m^2/s
Critical temperature of CO_2 ($T_{crt}^{CO_2}$)	304.13 K
Critical temperature of CH_4 ($T_{crt}^{CH_4}$)	190.564 K
Critical pressure of CO_2 ($p_{crt}^{CO_2}$)	7.3773×10^6 Pa
Critical pressure of CH_4 ($p_{crt}^{CH_4}$)	4.599×10^6 Pa
Tortuosity (τ)	5

Note: [1] From Edwards et al. (2015); [2] $D_0^{CH_4,sf}$ is from Guo et al. (2018), while $D_0^{CO_2,sf}$ is scaled from $D_0^{CH_4,sf}$ using molecular weight; [3] From Guevara-Carrion et al. (2019).
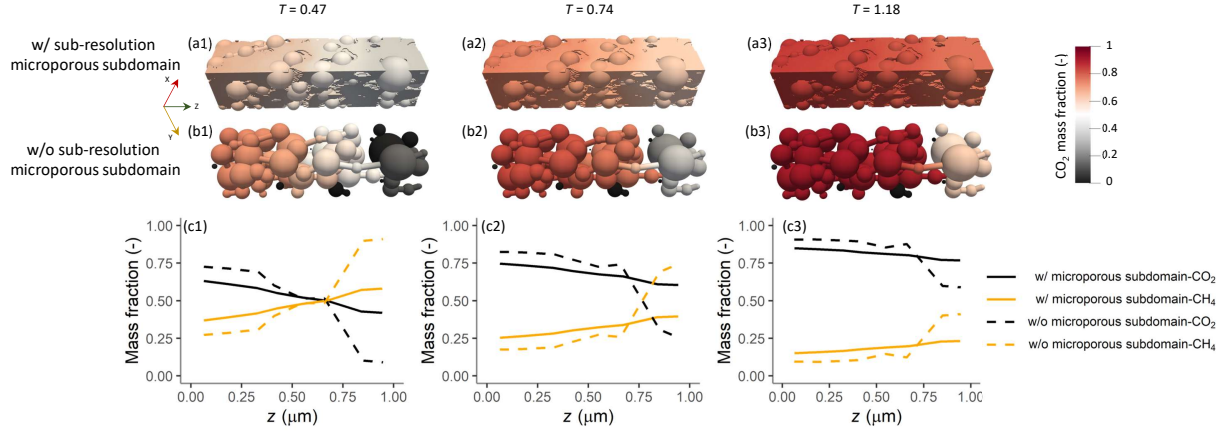
Figure 5: Simulated spatial distributions of CO_2 mass fraction at $T = 0.13$, 0.33 and 0.84 during CO_2 injection with (Subplots a1–a3) and without (Subplots b1–b3) including the sub-resolution microporous subdomain. Subplots c1–c3 show the cross-sectional average mass fractions along the z axis for CO_2 and CH_4 with and without accounting for the sub-resolution microporous subdomain. The simulations were conducted using the h-PNM-continuum model.

Figure 6: (a) The simulated mass flow rate of CO_2 and CH_4 with and without accounting for the sub-resolution microporous subdomain at the outlet boundary. (b) Simulated cumulative CH_4 production with and without accounting for the sub-resolution microporous subdomain. The simulations were conducted using the h-PNM-continuum model.
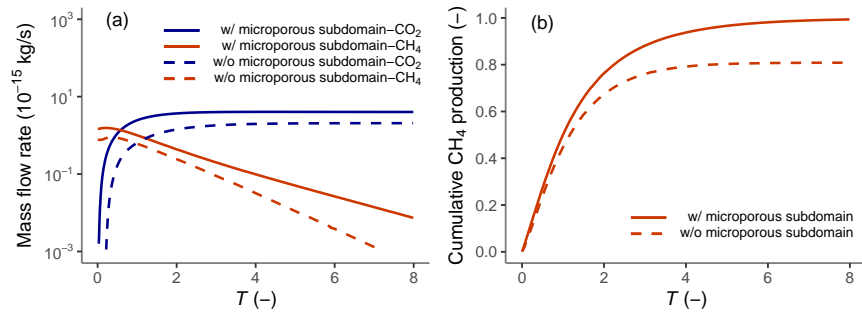
model), which indicates a quick invasion of CO_2 because of the improved effective connectivity through the entire domain. Besides, the mass flow rate of CH_4 in the h-PNM-continuum model is much higher than that simulated by the PNM model and declines much slower than the latter. Meanwhile, as is shown in Figure 6(b), the cumulative mass production of CH_4 from the whole domain is higher than the resolved pore subdomain. It indicates that the sub-resolution microporous subdomain can continuously serve as a significant source for CH_4 production—the CH_4 production can be as high as 19% of the whole domain. Our modeling results delineate the significant contribution of the continuum subdomain to the overall gas production.

4. Discussion

We have developed a new hybrid pore-network-continuum modeling framework (h-PNM-continuum) for simulating flow and transport in 3D multiscale pore structures. Our numerical experiments, spanning from steady-state single-phase flow, single-phase solute transport, and single-phase two-component gas transport, demonstrate that the h-PNM-continuum model can accurately simulate flow and transport processes and the mass transfer between the resolved pore and continuum subdomains, while being much more computationally efficient than the DNS method. Below, we compare the h-PNM-continuum model with other two-scale pore network models, comment on the computational efficiency and numerical accuracy of h-PNM-continuum model, and discuss how the h-PNM-continuum modeling framework may be extended to model two-phase flow in 3D multiscale pore structures.

4.1. Comparison with other "two-scale" models

We comment on how the h-PNM-continuum model relates to other "two-scale" network models reported in the literature (Bauer et al., 2012; Jiang et al., 2013; Mehmani & Prodanović, 2014; Bultreys et al., 2015; Prodanović et al., 2015), which we refer to as dual PNMs in the present study. The dual PNMs represent both the resolved pores and the sub-resolution microporous regions of a "two-scale" porous medium. The difference between the different dual PNMs lies in the specific approach for representing the microporous regions and their connectivity with the resolved pore space.

One common approach employed by the dual PNMs is to represent the sub-resolution microporous regions by smaller-scale pore networks. The smaller-scale pore networks can be stochastically generated or based on higher-resolution images that resolve the microporous regions. In Jiang et al. (2013), a small-scale pore network is stochastically generated and then combined with the larger-scale pore network. The dual PNM involves the following steps. (1) Two networks (i.e., the large-scale and small-scale networks) were firstly extracted from micro-CT images at different length scales using the Pore Analysis Tools (Jiang et al., 2007; Jiang, 2008). Then, (2) the statistic information from each pore network is used to reconstruct a stochastic network that is representative of the original one (Jiang et al., 2012). Finally, (3) the large-scale and small-scale networks are integrated into a single two-scale pore network by connecting the two networks using added small-scale bonds. Micropores were uniformly distributed in the remaining space excluding the regions occupied by the large-scale network, and the spatial correlations were not considered. In addition, the coupling of the two networks was based on a stochastic algorithm, which does not follow the specific connectivities in the 3D digital image. For the dual PNM by Prodanović et al. (2015), the smaller-scale pore network is constructed from digital images of microporous subdomains as follows: (1) Extract the large-scale pore network (i.e., macro-network) from the 3D digital images; (2) Identify the microporous regions in the images; (3) Rescale the small-scale pore network (i.e., micro-network) by a scaling factor to fit into the microporous regions; (4) Finally, connect the small-scale network to the larger-scale network to obtain a two-scale network model. In their study, a network element (e.g., a pore) in the network does not necessarily

19

correspond to a single pore space; rather, it can encapsulate the collective characteristics of a small-scale network within the microporous subregion. The dual PNMs discussed above can have a large number of network elements due to the presence of many sub-resolution small pores, which can lead to prohibitive computational costs even for a relatively small shale rock sample on the order of a few micrometers in each dimension.

Another approach that has been used by dual PNMs is to approximate the microporous regions as effective "pore throats" without resolving the pore structures of the microporous regions. Bauer et al. (2012) extracted the resolved pore network (i.e., coarse-scale pore network) from the digital images and assigned some portion of the resolved pores to be connected by micropores in parallel to the resolved pore throats. Bultreys et al. (2015) developed another image-based dual PNM, in which a resolved pore network is extracted from micro-CT images, and micropores are allowed to act both in parallel and in serial to the resolved pore network. To determine the connection between micropores and resolved pores, a special link (i.e., referred to as "micro-link" by the authors) is added if two pores in the resolved pore network touch the same microporous region. Otherwise, the micro-link does not exist, or it can be considered as solid. While the dual PNMs proposed by Bauer et al. (2012) and Bultreys et al. (2015) significantly reduce the computational cost relative to the dual PNMs discussed in the previous paragraph, they do not represent the actual location of the microporous regions and their specific connections with resolved pores.

The h-PNM-continuum model developed in the present study treats the micropores as a continuum using the Darcy-scale formalism and explicitly represents the flow and transport processes in the resolved pores using a pore network model. In the hybrid framework, the multiple scales originate directly from flow physics occurring at different scales, for example, the gas transport in micropores vs. resolved pores as described in Section 2.2.3. This hybrid approach significantly reduces the computational cost by representing the resolved pore space using PNM and modeling the sub-resolution microporous subdomain at the continuum scale.

4.2. Computational efficiency and numerical accuracy

The h-PNM-continuum model significantly reduces the computational cost relative to a DNS model. To evaluate the computational efficiency, we compare the number of numerical cells in the two models. The numerical cell numbers for a synthetic porous medium (Sections 3.1 & 3.2) and a shale sample (Section 3.3) are presented in Table 3. The number of numerical cells for the h-PNM-continuum model is over 99.9% smaller than that for the DNS model across all three test cases. While h-PNM-continuum still has a large number of numerical cells for the continuum subdomain (i.e., the same as that of the DNS model), the governing equation there is much simpler relative to that in the resolved pore subdomain for the DNS model. Numerical coarsening strategies may also be developed to reduce the number of numerical cells in the continuum subdomains, given that the flow and transport dynamics are anticipated to be much slower than that in the resolved pore subdomain.

While the h-PNM-continuum is much more computationally efficient than the DNS model, the approximation of representing the resolved pore space by a pore network introduces additional errors just like any

Table 3: Comparisons of the number of numerical cells used in the hybrid pore-network-continuum model and the DNS method.

Model		Synthetic porous medium	Typical shale sample
Resolved pore subdomain	h-PNM-continuum	509	76
	DNS method	1,110,198	153,095
Continuum subdomain	h-PNM-continuum	535,981	345,905
	DNS method		

other pore network models. In the present study, we employ a basic version of PNM to demonstrate the image-based hybrid framework for coupling a PNM with a continuum scale model. More advanced PNMs reported in the literature have significantly improved their predictive capabilities (Mehmani & Tchelepi, 2017; Raeini et al., 2017, 2018; Zhao et al., 2020). As discussed in Section 3.1, These enhanced PNM approaches can be incorporated into our h-PNM-continuum framework to further improve the accuracy.

4.3. Extension of the hybrid framework for other applications

In addition to the examples demonstrated in the present study, the h-PNM-continuum modeling framework can also be potentially generalized to model more complex processes in two-scale porous media, such as two-phase flow or reactive transport. Extending the h-PNM-continuum to model two-phase flow in two-scale porous media can be particularly attractive given that they are computationally expensive when simulated by DNS models. Here, we outline the conceptual steps for extending the h-PNM-continuum model for modeling two-phase flow in a two-scale porous medium. For the resolved pore subdomain, we may employ a dynamic PNM or a quasi-static PNM to represent the two-phase flow, depending on the question of interest. For instance, for the two-scale porous media where there is a significant contrast between the pore sizes of the resolve pore subdomain and the sub-resolution continuum subdomain, the two-phase flow in the resolved pore subdomain is expected to be much slower than that in the microporous region. In this case, it may be sufficient to use a quasi-static PNM for the resolved pore subdomain. The quasi-static distribution of the two fluid phases can be updated based on the fluxes at the interfaces between the resolved pore subdomain and the continuum subdomain. For the continuum subdomain, we can employ the standard two-phase flow model at the continuum scale. The two-phase flow properties of the microporous region (i.e., capillary pressure as a function of phase saturation and relative permeability function) may be estimated from higher-resolution images or pore-size distribution information (e.g., obtained by mercury intrusion or nitrogen adsorption).

5. Conclusion

We have developed an image-based hybrid pore-network-continuum (h-PNM-continuum) modeling framework for the flow and transport processes in two-scale porous media. The hybrid framework treats the unresolved microporous region as a continuum and models the flow and transport at the Darcy scale, while

explicitly representing the flow and transport processes in the larger pores through a computationally efficient pore network model. The h-PNM-continuum modeling framework couples the pore network with the microporous subdomain based on the original connectivity between the two subdomains from 3D digital images.

We have validated the modeling framework by comparing it to DNS methods in a set of numerical experiments including steady-state incompressible single-phase flow and solute transport. The results suggest that the h-PNM-continuum model can accurately predict the overall flow and transport process and the mass transfer between the resolved pores and the sub-resolution microporous subdomains while being much more computationally efficient than the DNS methods. We have then demonstrated the applicability of the hybrid model for simulating two-component gas transport in shale rocks using the displacement of CH_4 by CO_2 as an example. The simulations illustrate the significant contribution of the continuum subdomain to the overall gas production. While the present study focuses on single-phase flow and transport, the h-PNM-continuum modeling framework may also be further extended to simulate more complex processes that involve multiphase flow, reactive transport, and non-Newtonian displacement. If desired, more advanced PNM approaches can also be incorporated into the h-PNM-continuum modeling framework to further improve the accuracy of representing flow and transport processes in the resolved pore subdomain.

List of variables

Name	Definition
Subscript i or j	Pore body labeled i or j.
Subscript m	The grid cell in the continuum subdomain.
Subscript ij	Pore throat ij between pore bodies i and j.
Subscript i,m	The connection between pore body i and the connected continuum cell m.
Subscript m,i	The connection between continuum cell m and the connected pore body i.
Superscript b	Bulk gas (i.e., the mixture of CO_2 or CH_4).
Superscript ads	Adsorption.
Superscript ex	Excess adsorption.
Superscript adv	Advection.
Superscript $disp$	Dispersion.
Superscript sf	Surface diffusion.
A_{ij}	The cross-sectional area of the pore throat ij (m^2).
$A_{i,m}$	Area of the interface between pore body i and continuum cell m (m^2).
C_i	Concentration in pore body i (kg/m^3).
C_{ij}	Concentration in pore throat ij (kg/m^3).
C_j	Concentration in pore body j (kg/m^3).

Name	Definition
D_0	The molecular diffusion coefficient (m^2/s).
$D_0^{CO_2,sf}$	Surface diffusion coefficient of CO_2 on flat solid surface (m^2/s).
$D_0^{CH_4,sf}$	Surface diffusion coefficient of CH_4 on flat solid surface (m^2/s).
$D_m^{CH_4,sf}$	Surface diffusion coefficient of CH_4 in the continuum subdomain (m^2/s).
$D_m^{CO_2,sf}$	Surface diffusion coefficient of CO_2 in the continuum subdomain (m^2/s).
$D_{ij}^{CO_2,disp}$	The dispersion coefficient of CO_2 in the pore throat ij (m^2/s).
$D_m^{CO_2,disp}$	The dispersion coefficient of CO_2 in the continuum subdomain (m^2/s).
$D_{i,m}^{CO_2,disp}$	The molecular diffusion coefficient of CO_2 at the interface between pore body i and continuum cell m (m^2/s).
d_{ij}	Diameter of the pore throat ij (m).
ϕ_m	Porosity (–).
$f(Kn)$	The correction factor (–).
$\Gamma_m^{CH_4,ex}$	Excess adsorption of CH_4 per unit volume of porous material (kg/m^3).
$\Gamma_m^{CO_2,ex}$	Excess adsorption of CO_2 per unit volume of porous material (kg/m^3).
$\Gamma_{m,max}^{CH_4}$	Maximum adsorption of CH_4 (kg/m^3).
$\Gamma_{m,max}^{CO_2}$	Maximum adsorption of CO_2 (kg/m^3).
g_{ij}	The conductance between pore bodies i and j ($m^4 \cdot$ s/kg).
$\mathcal{J}_{ij}^b$	Mass flux of bulk gas from pore body i to pore body j (kg/s).
$\mathcal{J}_{i,m}^b$	Mass flux of bulk gas from pore body i to continuum cell m (kg/s).
$\mathcal{J}_{m,i}^b$	Mass flux of bulk gas from continuum cell m to pore body i (kg/s).
$\mathcal{J}_{ij}^{CO_2,adv}$	Advective mass flux of CO_2 from pore body i to pore body j (kg/s).
$\mathcal{J}_{ij}^{CO_2,disp}$	Dispersive mass flux of CO_2 from pore body i to pore body j (kg/s).
$\mathcal{J}_{i,m}^{CO_2}$	Mass flux of CO_2 from pore body i to continuum cell m (kg/s).
$\mathcal{J}_{m,i}^{CO_2}$	Mass flux of CO_2 from continuum cell m to pore body i (kg/s).
J_m^b	Mass flux of bulk gas at the interfaces between continuum cell m and adjacent cells (kg/s/m^2).
$J_m^{CO_2,adv}$	Advective mass fluxes of CO_2 at the interfaces between continuum cell m and adjacent cells (kg/s/m^2).
$J_m^{CO_2,disp}$	Dispersive mass fluxes of CO_2 at the interfaces between continuum cell m and adjacent cells (kg/s/m^2).
$J_m^{CH_4,sf}$	Mass flux of CH_4 by surface diffusion (kg/s/m^2).
$J_m^{CO_2,sf}$	Mass flux of CO_2 by surface diffusion (kg/s/m^2).
$K_m^{CH_4}$	The Langmuir coefficient of CH_4 ($m \cdot s^2$/kg).
$K_m^{CO_2}$	The Langmuir coefficient of CO_2 ($m \cdot s^2$/kg).
k_m	Permeability (m^2).

Name	Definition
λ	The mean free path (m).
L	A characteristic length scale for gas flow (m).
l_{ij}	Length of the pore throat ij (m).
$l_{i,m}$	Distance between pore body i and continuum cell m (m).
μ_m	Fluid viscosity (Pa $\cdot$ s).
M_i	Number of continuum cells connected to pore body i (–).
M^b	Molar mass of the bulk gas (kg/mol).
M^{CH_4}	Molar mass of CH_4 (kg/mol).
M^{CO_2}	Molar mass of CO_2 (kg/mol).
N_i	Number of pore bodies connected to pore body i (–).
Ω_m	The domain of integration.
ω^{CH_4}	Mass fraction of CH_4 (–).
ω^{CO_2}	Mass fraction of CO_2 (–).
$\omega^{CH_4,ads}$	Mass fraction of CH_4 in the adsorbed phase (–).
$\omega^{CO_2,ads}$	Mass fraction of CO_2 in the adsorbed phase (–).
p	Pressure (Pa).
Pe	Local Peclet number (–).
p_r	The reduced pressure (–).
p_{crt}	The critical pressure (Pa).
$p_{crt}^{CO_2}$	The critical pressure of CO_2 (Pa).
$p_{crt}^{CH_4}$	The critical pressure of CH_4 (Pa).
ϖ^{CO_2}	Mole fraction of CO_2.
ϖ^{CH_4}	Mole fraction of CH_4.
$q_{i,m}$	The volumetric flux between pore body i and continuum cell m (m^3/s).
$q_{m,i}$	The volumetric flux between continuum cell m and pore body i (m^3/s).
ρ^{ads}	Adsorbed gas density kg/m^3).
ρ^b	Bulk gas density (kg/m^3).
R	The universal gas constant (kg $\cdot$ m^2/s^2/K/mol).
T	Temperature (K).
T_r	The reduced temperature (–).
T_{crt}	The critical temperature (K).
$T_{crt}^{CO_2}$	The critical temperature of CO_2 (K).
$T_{crt}^{CH_4}$	The critical temperature of CH_4 (K).
V_m	Volume of continuum cell (m^3).
V_i	Pore volume of pore body i (m^3).

Name	Definition
W_i	Number of pore bodies connected to continuum cell m (–).
ξ	A constant for dispersion in a cylindrical tube.
Z	The compressibility factor (–).

References

Bauer, D., Youssef, S., Fleury, M., Bekri, S., Rosenberg, E., & Vizika, O. (2012). Improving the estimations of petrophysical transport behavior of carbonate rocks using a dual pore network approach combined with computed microtomography. *Transport in porous media*, *94*, 505–524.

Bekri, S., Laroche, C., & Vizika, O. (2005). Pore network models to calculate transport and electrical properties of single or dual-porosity rocks. In *SCA* (p. 2005). volume 35.

Beskok, A., & Karniadakis, G. E. (1999). Report: a model for flows in channels, pipes, and ducts at micro and nano scales. *Microscale thermophysical engineering*, *3*, 43–77.

Blunt, M. J., Bijeljic, B., Dong, H., Gharbi, O., Iglauer, S., Mostaghimi, P., Paluszny, A., & Pentland, C. (2013). Pore-scale imaging and modelling. *Advances in Water resources*, *51*, 197–216.

Bultreys, T., De Boever, W., & Cnudde, V. (2016). Imaging and image-based fluid transport modeling at the pore scale in geological materials: A practical introduction to the current state-of-the-art. *Earth-Science Reviews*, *155*, 93–128.

Bultreys, T., Van Hoorebeke, L., & Cnudde, V. (2015). Multi-scale, micro-computed tomography-based pore network models to simulate drainage in heterogeneous rocks. *Advances in Water resources*, *78*, 36–49.

Carrillo, F. J., & Bourg, I. C. (2019). A darcy-brinkman-biot approach to modeling the hydrology and mechanics of porous media containing macropores and deformable microporous regions. *Water Resources Research*, *55*, 8096–8121.

Carrillo, F. J., & Bourg, I. C. (2021). Modeling multiphase flow within and around deformable porous materials: A darcy-brinkman-biot approach. *Water Resources Research*, *57*, e2020WR028734.

Carrillo, F. J., Bourg, I. C., & Soulaine, C. (2020). Multiphase flow modeling in multiscale porous media: An open-source micro-continuum approach. *Journal of Computational Physics: X*, *8*, 100073.

Carrillo, F. J., Soulaine, C., & Bourg, I. C. (2022). The impact of sub-resolution porosity on numerical simulations of multiphase flow. *Advances in Water Resources*, *161*, 104094.

Cnudde, V., & Boone, M. N. (2013). High-resolution x-ray computed tomography in geosciences: A review of the current technology and applications. *Earth-Science Reviews*, *123*, 1–17.

Edwards, R. W., Celia, M. A., Bandilla, K. W., Doster, F., & Kanno, C. M. (2015). A model to estimate carbon dioxide injectivity and storage capacity for geological sequestration in shale gas wells. *Environmental science & technology*, *49*, 9222–9229.

Elmorsy, M., El-Dakhakhni, W., & Zhao, B. (2023). Rapid permeability upscaling of digital porous media via physics-informed neural networks. *Water Resources Research*, *59*, e2023WR035064.

Golfier, F., Zarcone, C., Bazin, B., Lenormand, R., Lasseux, D., & Quintard, M. (2002). On the ability of a darcy-scale model to capture wormhole formation during the dissolution of a porous medium. *Journal of fluid Mechanics*, *457*, 213–254.

Gong, Y., Sedghi, M., & Piri, M. (2021). Two-phase relative permeability of rough-walled fractures: A dynamic pore-scale modeling of the effects of aperture geometry. *Water Resources Research*, *57*, e2021WR030104.

Gostick, J. T. (2017). Versatile and efficient pore network extraction method using marker-based watershed segmentation. *Physical Review E*, *96*, 023307.

Guevara-Carrion, G., Ancherbak, S., Mialdun, A., Vrabec, J., & Shevtsova, V. (2019). Diffusion of methane in supercritical carbon dioxide across the widom line. *Scientific reports*, *9*, 8466.

Guo, B., Ma, L., & Tchelepi, H. A. (2018). Image-based micro-continuum model for gas flow in organic-rich shale rock. *Advances in Water Resources*, *122*, 70–84.

Guo, B., Mehmani, Y., & Tchelepi, H. A. (2019). Multiscale formulation of pore-scale compressible darcy-stokes flow. *Journal of Computational Physics*, *397*, 108849.

Heller, R., & Zoback, M. (2014). Adsorption of methane and carbon dioxide on gas shale and pure mineral samples. *Journal of unconventional oil and gas resources*, *8*, 14–24.

Jiang, Z. (2008). *Quantitative characterisation of the geometry and topology of pore space in 3D rock images*. Ph.D. thesis Heriot-Watt University.

Jiang, Z., Van Dijke, M., Sorbie, K. S., & Couples, G. D. (2013). Representation of multiscale heterogeneity via multiscale pore networks. *Water resources research*, *49*, 5437–5449.

Jiang, Z., Van Dijke, M., Wu, K., Couples, G. D., Sorbie, K. S., & Ma, J. (2012). Stochastic pore network generation from 3d rock images. *Transport in porous media*, *94*, 571–593.

Jiang, Z., Wu, K., Couples, G., Van Dijke, M. I. J., Sorbie, K. S., & Ma, J. (2007). Efficient extraction of networks from three-dimensional porous media. *Water resources research*, *43*.

Lee, A. L., Gonzalez, M. H., & Eakin, B. E. (1966). The viscosity of natural gases. *Journal of petroleum technology*, *18*, 997–1000.

Lie, K.-A. (2019). *An introduction to reservoir simulation using MATLAB/GNU Octave: User guide for the MATLAB Reservoir Simulation Toolbox (MRST)*. Cambridge University Press.

Maes, J., & Menke, H. P. (2021). Geochemfoam: Direct modelling of multiphase reactive transport in real pore geometries with equilibrium reactions. *Transport in Porous Media*, *139*, 271–299.

Maes, J., & Menke, H. P. (2022). Geochemfoam: Direct modelling of flow and heat transfer in micro-ct images of porous media. *Heat and Mass Transfer*, *58*, 1937–1947.

Maes, J., Soulaine, C., & Menke, H. P. (2022). Improved volume-of-solid formulations for micro-continuum simulation of mineral dissolution at the pore-scale. *Frontiers in Earth Science*, *10*, 917931.

Mahmoud, M. (2014). Development of a new correlation of gas compressibility factor (z-factor) for high pressure gas reservoirs. *Journal of Energy Resources Technology*, *136*.

Meakin, P., & Tartakovsky, A. M. (2009). Modeling and simulation of pore-scale multiphase fluid flow and reactive transport in fractured and porous media. *Reviews of Geophysics*, *47*.

Mehmani, A., & Prodanović, M. (2014). The effect of microporosity on transport properties in porous media. *Advances in Water Resources*, *63*, 104–119.

Mehmani, Y., Anderson, T., Wang, Y., Aryana, S. A., Battiato, I., Tchelepi, H. A., & Kovscek, A. R. (2021). Striving to translate shale physics across ten orders of magnitude: What have we learned? *Earth-Science Reviews*, *223*, 103848.

Mehmani, Y., & Tchelepi, H. A. (2017). Minimum requirements for predictive pore-network modeling of solute transport in micromodels. *Advances in water resources*, *108*, 83–98.

Molins, S., Soulaine, C., Prasianakis, N. I., Abbasi, A., Poncet, P., Ladd, A. J., Starchenko, V., Roman, S., Trebotich, D., Tchelepi, H. A. et al. (2021). Simulation of mineral dissolution at the pore scale with evolving fluid-solid interfaces: Review of approaches and benchmark problem set. *Computational Geosciences*, *25*, 1285–1318.

Prodanović, M., Mehmani, A., & Sheppard, A. P. (2015). Imaged-based multiscale network modelling of microporosity in carbonates. *Geological Society, London, Special Publications*, *406*, 95–113.

Rabbani, A., Jamshidi, S., & Salehi, S. (2014). An automated simple algorithm for realistic pore network extraction from micro-tomography images. *Journal of Petroleum Science and Engineering*, *123*, 164–171.

Raeini, A. Q., Bijeljic, B., & Blunt, M. J. (2017). Generalized network modeling: Network extraction as a coarse-scale discretization of the void space of porous media. *Physical Review E*, *96*, 013312.

Raeini, A. Q., Bijeljic, B., & Blunt, M. J. (2018). Generalized network modeling of capillary-dominated two-phase flow. *Physical Review E*, *97*, 023308.

Scheibe, T. D., Perkins, W. A., Richmond, M. C., McKinley, M. I., Romero-Gomez, P. D., Oostrom, M., Wietsma, T. W., Serkowski, J. A., & Zachara, J. M. (2015). Pore-scale and multiscale numerical simulation of flow and transport in a laboratory-scale column. *Water Resources Research*, *51*, 1023–1035.

Soulaine, C., Creux, P., & Tchelepi, H. A. (2019). Micro-continuum framework for pore-scale multiphase fluid transport in shale formations. *Transport in Porous Media*, *127*, 85–112.

Soulaine, C., Gjetvaj, F., Garing, C., Roman, S., Russian, A., Gouze, P., & Tchelepi, H. A. (2016). The impact of sub-resolution porosity of x-ray microtomography images on the permeability. *Transport in porous media*, *113*, 227–243.

Soulaine, C., Roman, S., Kovscek, A., & Tchelepi, H. A. (2017). Mineral dissolution and wormholing from a pore-scale perspective. *Journal of Fluid Mechanics*, *827*, 457–483.

Soulaine, C., Roman, S., Kovscek, A., & Tchelepi, H. A. (2018). Pore-scale modelling of multiphase reactive flow: application to mineral dissolution with production of CO_2. *Journal of Fluid Mechanics*, *855*, 616–645.

Soulaine, C., & Tchelepi, H. A. (2016). Micro-continuum approach for pore-scale simulation of subsurface processes. *Transport in Porous Media*, *113*, 431–456.

Taylor, G. I. (1953). Dispersion of soluble matter in solvent flowing slowly through a tube. *Proceedings of the Royal Society of London. Series A. Mathematical and Physical Sciences*, *219*, 186–203.

de Vries, E. T., Raoof, A., & van Genuchten, M. T. (2017). Multiscale modelling of dual-porosity porous media; a computational pore-scale study for flow and solute transport. *Advances in water resources*, *105*, 82–95.

Wildenschild, D., & Sheppard, A. P. (2013). X-ray imaging and analysis techniques for quantifying pore-scale structure and processes in subsurface porous medium systems. *Advances in Water resources*, *51*, 217–246.

Xiong, Q., Baychev, T. G., & Jivkov, A. P. (2016). Review of pore network modelling of porous media: Experimental characterisations, network constructions and applications to reactive transport. *Journal of contaminant hydrology*, *192*, 101–117.

Xu, Q., Dai, X., Yang, J., Liu, Z., & Shi, L. (2022). Image-based modelling of coke combustion in a multiscale porous medium using a micro-continuum framework. *Journal of Fluid Mechanics*, *932*, A51.

Yang, X., Mehmani, Y., Perkins, W. A., Pasquali, A., Schönherr, M., Kim, K., Perego, M., Parks, M. L., Trask, N., Balhoff, M. T. et al. (2016). Intercomparison of 3d pore-scale flow and solute transport simulation methods. *Advances in water resources*, *95*, 176–189.

Yang, X., Sun, H., Yang, Y., Liu, Y., & Li, X. (2021). Recent progress in multi-scale modeling and simulation of flow and solute transport in porous media. *Wiley Interdisciplinary Reviews: Water*, *8*, e1561.

You, J., & Lee, K. J. (2021). Analyzing the dynamics of mineral dissolution during acid fracturing by pore-scale modeling of acid-rock interaction. *SPE Journal*, *26*, 639–652.

Zahasky, C., Murugesu, M. P., Kurotori, T., Sutton, C., Druhan, J. L., Vega, B., Benson, S. M., & Kovscek, A. R. (2023). Quantification of the impact of acidified brine on fracture-matrix transport in a naturally fractured shale using in situ imaging and modeling. *Energy & Fuels*, *37*, 12101–12112.

Zhang, P., Celia, M. A., Bandilla, K. W., Hu, L., & Meegoda, J. N. (2020). A pore-network simulation model of dynamic co 2 migration in organic-rich shale formations. *Transport in Porous Media*, *133*, 479–496.

Zhang, T., Ellis, G. S., Ruppel, S. C., Milliken, K., & Yang, R. (2012). Effect of organic-matter type and thermal maturity on methane adsorption in shale-gas systems. *Organic geochemistry*, *47*, 120–131.

Zhao, J., Qin, F., Derome, D., & Carmeliet, J. (2020). Simulation of quasi-static drainage displacement in porous media on pore-scale: Coupling lattice boltzmann method and pore network model. *Journal of Hydrology*, *588*, 125080.

Zheng, J., Wang, Z., Gong, W., Ju, Y., & Wang, M. (2017). Characterization of nanopore morphology of shale and its effects on gas permeability. *Journal of Natural Gas Science and Engineering*, *47*, 83–90.